# From spikes to intercellular waves: tuning intercellular $Ca^{2+}$ signaling dynamics modulates organ size control

**Dharsan K. Soundarrajan[1, ¶], Francisco J. Huizar[1,2, ¶], Ramezan Paravitorghabeh[1, ¶], Trent Robinett[1], Jeremiah J. Zartman[1,2*]**

[1]Department of Chemical and Biomolecular Engineering, University of Notre Dame, South Bend, Indiana

[2]Bioengineering Graduate Program, University of Notre Dame, South Bend, Indiana

[¶]These authors contributed equally

[*]Correspondence: jzartman@nd.edu

**Abstract**

Information flow within and between cells depends in part on calcium ($Ca^{2+}$) signaling dynamics. However, the biophysical mechanisms that govern emergent patterns of $Ca^{2+}$ signaling dynamics at the organ level remain elusive. Recent experimental studies in developing *Drosophila* wing imaginal discs demonstrate the emergence of four distinct patterns of $Ca^{2+}$ activity: $Ca^{2+}$ spikes, intercellular $Ca^{2+}$ transients, tissue-level $Ca^{2+}$ waves, and a global "fluttering" state. Here, we used a combination of computational modeling and experimental approaches to identify two different populations of cells within tissues that are connected by gap junctional proteins. We term these two subpopulations "initiator cells" defined by elevated levels of Phospholipase C (PLC) activity and "standby cells," which exhibit baseline activity. We found that the strength of hormonal stimulation and extent of gap junctional communication jointly determine the predominate class of $Ca^{2+}$ signaling activity. Further, single-cell $Ca^{2+}$ spikes are stimulated by insulin, while intercellular $Ca^{2+}$ waves depend on Gαq activity. Our computational model successfully recapitulates how the dynamics of $Ca^{2+}$ transients varies during organ growth. Phenotypic analysis of perturbations to Gαq and insulin signaling support an integrated model of cytoplasmic $Ca^{2+}$ as a dynamic reporter of overall tissue growth. Further, we show that perturbations to $Ca^{2+}$ signaling tune the final size of organs. This work provides a platform to further study how organ size regulation emerges from the crosstalk between biochemical growth signals and heterogeneous cell signaling states.

**Author Summary**

Calcium ($Ca^{2+}$) is a universal second messenger that regulates a myriad of cellular processes such as cell division, cell proliferation and apoptosis. Multiple patterns of $Ca^{2+}$ signaling including single cell spikes, multicellular $Ca^{2+}$ transients, large-scale $Ca^{2+}$ waves, and global "fluttering" have been observed in epithelial systems during organ development. Key molecular players and biophysical mechanisms involved in formation of these patterns during organ development are not well understood. In this work, we developed a generalized multicellular model of $Ca^{2+}$ that captures all the key categories of $Ca^{2+}$ activity as a function of key hormonal signals. Integration of model predictions and experiments reveals two subclasses of cell populations and demonstrates that $Ca^{2+}$ signaling activity at the organ scale is defined by a general decrease in gap junction communication as organ growth. Our experiments also reveal that a "goldilocks zone" of optimal $Ca^{2+}$ activity is required to achieve optimal growth at the organ level.

## Introduction

Epithelial cells do not observe social distancing. This is evident during epithelial morphogenesis when cells communicate and coordinate their activities to generate functioning organs (Leptin, 1995; Schöck and Perrimon, 2002). One modality of intercellular communication occurs through gap junctions (GJ), intercellular channels that permit direct cell-cell transfer of ions and other small molecules (Levin, 2007). Calcium ions ($Ca^{2+}$) act as second messengers that regulate a myriad of cellular processes such as proliferation, differentiation, transcription, metabolism, cellular motility, fertilization, and neuronal communication (Berridge, 2005; Carafoli, 2002; Clapham, 2007; Cuthbertson and Cobbold, 1985; Giorgi et al., 2018; Humeau et al., 2017; La Rovere et al., 2016; Martin and Bernard, 2017; Orrenius et al., 2003; Wei et al., 2009). $Ca^{2+}$ signaling also regulates developmental processes at the multicellular level. For instance, $Ca^{2+}$ signaling has been shown to regulate scale development in butterfly wings (Ohno and Otaki, 2015). It also mediates autophagic and apoptotic processes required for hearing acquisition in the developing cochlea (Ceriani et al., 2016; Mammano and Bortolozzi, 2018; Takeuchi et al., 2020). However, a systems-level description of $Ca^{2+}$ signaling during organ development is lacking.

A major challenge in reverse engineering $Ca^{2+}$ signaling during organ development is the lack of an in vivo model system to identify how cells interpret and integrate information across the broad range of input molecules that dynamically vary concentrations of cytosolic $Ca^{2+}$ ions. In particular, it remains unclear how single-cell $Ca^{2+}$ dynamics are coordinated to regulate tissue-level $Ca^{2+}$ patterns. To overcome these challenges, we developed a computational model based on a realistic geometry of epithelial cells to model $Ca^{2+}$ signaling in the *Drosophila* wing imaginal disc. The *Drosophila* wing imaginal disc is an experimentally amenable system for investigating systems-level regulation of cell signaling (Figure 1A) (Balaji et al., 2017; Brodskiy et al., 2019; Restrepo and Basler, 2016). *Drosophila* wing imaginal discs are a premier system to gain insights into several organ-intrinsic and organ-extrinsic mechanisms that control organ growth (Buchmann

106 et al., 2014; Gou et al., 2020; Hariharan, 2015; Restrepo et al., 2014; Vollmer and Iber, 2016;
107 Vollmer et al., 2017).

108 Previous experimental investigations revealed four classes of $Ca^{2+}$ signaling activity in the
109 developing wing disc: single-cell $Ca^{2+}$ spikes, multicellular transients, intercellular waves, and
110 global fluttering (Figure 1B, C). Recently we showed that these patterns depend on the strength
111 of agonist stimulation (Brodskiy et al., 2019). We and others have previously reported that $Ca^{2+}$
112 patterns observed in the wing disc are dependent on phospholipase C (PLC) and the inositol
113 trisphosphate receptor ($IP_3R$) pathway mediated by gap junctional communication (Balaji et al.,
114 2017; Brodskiy et al., 2019; Restrepo and Basler, 2016). In non-excitable cells, stimulation of
115 receptors in the cell surface results in activation of PLCs to generate $IP_3$, which binds to and
116 activates $IP_3R$ (Figure 1D) (Clapham, 2007). Upon binding, $IP_3Rs$ channel $Ca^{2+}$ from the
117 endoplasmic reticulum (ER) to the cytosolic space (Berridge, 1987; Berridge et al., 2000;
118 Clapham, 2007). However, the specific receptors involved in stimulation of PLCs in the *Drosophila*
119 wing imaginal disc remain to be more fully defined. The key physical/chemical parameters and
120 their interactions that define multicellular $Ca^{2+}$ dynamics in response to agonist stimulation is not
121 fully characterized. How these different spatiotemporal modes of signaling encode information
122 from upstream signals to impact downstream cellular processes during organ development is not
123 characterized. We have previously shown that inhibition of $Ca^{2+}$ regulators $IP_3R$, PLC21C, Gαq
124 and gap junctional protein innexin 2 (Inx2) in the wing disc results in reduction in size of adult
125 wing blade (Brodskiy et al., 2019). Whether changes to multiscale $Ca^{2+}$ signaling patterns in wing
126 disc alters overall adult blade wing size remains unknown.

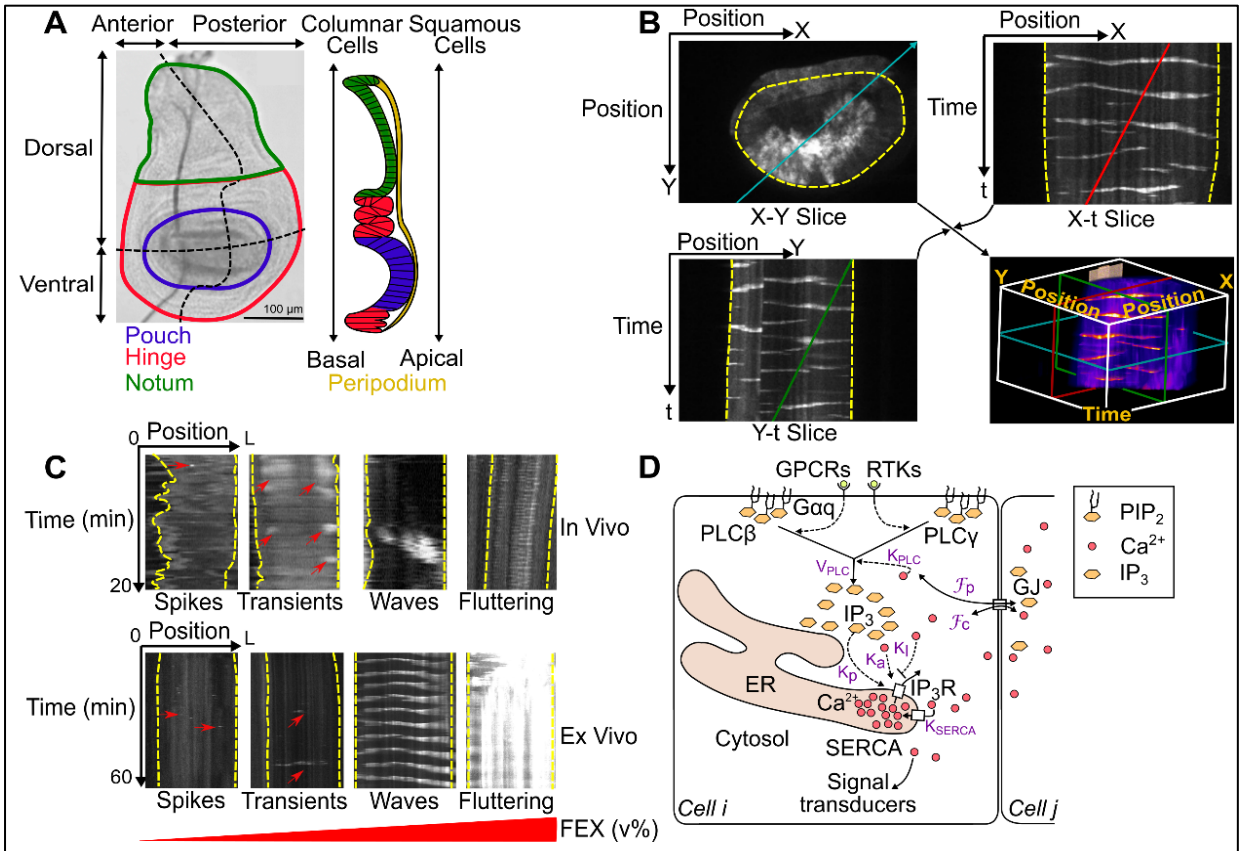


**E**

| Variable description | Defining equations |
|---|---|
| Cytosolic [$Ca^{2+}$] and [$IP_3$] intercellular flux | $Flux\ of\ species\ m = J_m \approx \mathcal{F}_m \left[ \sum_{j \in N_i} m_j l_j - m_j \left( \sum_{j \in N_i} l_j \right) \right]$ |
| Cytosolic [$Ca^{2+}$] denoted by (c) | $\frac{dc}{dt} = J_c + \left[ k_1 \left( r \frac{c}{K_a + c} \frac{p}{K_p + p} \right)^3 + k_2 \right] (s - c) - V_{serca} \frac{c^2}{c^2 + K_{serca}^2}$ |
| Cytosolic [$IP_3$] denoted by (p) | $\frac{dp}{dt} = J_p + V_{PLC} \frac{c^2}{c^2 + K_{PLC}^2} + k_{5P}\, p$ |
| ER [$Ca^{2+}$] denoted by (s) | $s(t) = \frac{c_{tot} - c(t)}{\beta}$ |
| Fraction of inactivated $IP_3$ receptors denoted by (r) | $\frac{dr}{dt} = \frac{1}{\tau_{max}} \frac{k_\tau^4 + c^4}{k_\tau^4} (1 - r \frac{K_i + c}{K_i})$ |

**Figure 1: Multicellular $Ca^{2+}$ signaling in a developing organ. (A)** (*Left panel*) Image of third instar *Drosophila* wing imaginal disc. The larval wing disc includes four regions: pouch (blue), hinge (red), notum (green) and peripodium (yellow). The pouch cells are the region of interest for this study. (*Right panel*) A schematic of the side view of the wing disc showing the peripodial membrane composed of squamous epithelial cells. **(B)** Kymographs illustrate two-dimensional slices of three-dimensional (X, Y and t planes respectively) spatiotemporal signaling. $Ca^{2+}$ signaling activity is related to the fluorescence intensity of the GCaMP6f sensor. A line in the X-Y plane (blue), the X-t plane (red), and Y-t plane (green) are overlaid to illustrate the positions of 2D projections in 3D data set. **(C)** Four classes of $Ca^{2+}$ signaling patterns are observed both in vivo and ex vivo: single-cell spikes, intercellular transient, intercellular waves and fluttering (Brodskiy et al., 2019). In ex vivo cultures, the occurrence of these patterns depend on the concentration of fly extract added to the culture media. Red arrows highlight subtle cellular $Ca^{2+}$ activity. **(D)** Major components of $Ca^{2+}$ toolkit: G protein–coupled receptors (GPCR), receptor tyrosine kinase (RTK), gap

junctions (GJ), Inositol trisphosphate ($IP_3$), diacylglycerol (DAG), Phospholipase C (PLC), Phosphatidylinositol 4,5-bisphosphate ($PIP_2$), sarco/endoplasmic reticulum $Ca^{2+}$-ATPase (SERCA) and $IP_3$ receptors ($IP_3R$). Parameters for our computational model are denoted in purple. $K_{PLC}$ values are presumably a function of the specific PLC isoforms active in the cell. **(E)** A summary of baseline $Ca^{2+}$ signaling model. More details on each dynamical equation and meaning of the parameters in the model are described in Supporting Information and text.

Overall, the computational models of calcium signaling in developing epithelial systems have to date received sparse attention. Here, we report the necessary conditions to generate the full spectrum of experimentally observed spatiotemporal patterns by employing a computational modeling approach. To do so, we built a geometrically accurate 2D-model of a wing disc based on experimental data. We discovered that in silico replication of wing disc $Ca^{2+}$ patterns requires two distinct classes of cells, which we term as “initiator cells” and “standby cells.” We show how the standby cells organize themselves with respect to a $V_{PLC}$ Hopf bifurcation threshold, and how the range of standby cell $V_{PLC}$ values determine the final patterns of $Ca^{2+}$ signaling. Next, computational simulations and experiments demonstrate that gap junctional communication alters $Ca^{2+}$ signaling response resulting in more $Ca^{2+}$ spikes in the absence of external stimuli. Finally, we provide computational and experimental evidence for the role of $Ca^{2+}$ signaling in imaginal disc morphogenesis. Our findings suggest a “goldilocks zone” of $Ca^{2+}$ where lower levels of $Ca^{2+}$ is correlated with reduced organ growth and higher levels of $Ca^{2+}$ is also correlated with reduced growth dependent upon the stimulus triggering the $Ca^{2+}$ signal. Overall, we identify crucial crosstalk between biochemical growth signals, such as insulin and Gαq, and heterogeneous cell signaling states during the growth of an organ.

## Results

### Relative rate of $IP_3$ production governs transitions between classes of spatiotemporal $Ca^{2+}$ patterns at the tissue level

167 Multiple spatiotemporal classes of $Ca^{2+}$ activity are observed in vivo and ex vivo in the
168 wing disc. However, an understanding of how this activity is regulated requires developing a
169 systems-level description. To summarize, these include: (i) single-cell $Ca^{2+}$ spikes, (ii) intercellular
170 $Ca^{2+}$ transients (ICTs), (iii) intercellular $Ca^{2+}$ waves (ICWs), and a (iv) global fluttering
171 phenomenon (Figure 1C, Table S1, SI videos 1-8) (Balaji et al., 2017; Brodskiy et al., 2019;
172 Restrepo and Basler, 2016). The frequencies of these observed classes are dependent on the
173 age of the larvae in both in vivo and ex vivo experiments. Younger larva with smaller discs (4-5
174 days after egg laying) exhibit higher occurrences of ICWs and fluttering states while older, larger
175 larval discs (6-8 days after egg laying) predominantly show ICTs and spikes (Brodskiy et al.,
176 2019). For ex vivo cultures, the transition from limited to tissue-wide calcium activity depends on
177 the amount of fly extract (FEX) added to the culture. Low concentrations of FEX stimulated $Ca^{2+}$
178 spikes. Progressively increasing levels of FEX resulted in ICTs, ICWs, and eventually fluttering.
179 Further, FEX-stimulated $Ca^{2+}$ dynamics is based on $IP_3R$-based release of $Ca^{2+}$ from the ER to
180 the cytosol as shown in Figure 1D (Brodskiy et al., 2019).

181 These experimental findings motivated us to ask what specific cellular properties of the
182 wing disc result in the emergence of these distinct patterns. To systematically investigate the
183 underlying principles governing the emergence of these patterns, we formulated a two-
184 dimensional image-based geometrically realistic computational model of $Ca^{2+}$ signaling in the
185 wing disc pouch where the columnar epithelial cells are connected by gap junctions (Figure S1),
186 (Jursnich et al., 1990; Ryerse, 1982; Weir and Lo, 1982, 1985). Image-based modelling enables
187 the wholistic characterization of molecular mechanisms and tissue dynamics during
188 organogenesis (Gómez et al., 2017). Given the near universal conservation of the $Ca^{2+}$ signaling
189 pathway across model systems (Berridge, 1987; Berridge et al., 2000), the baseline single-cell
190 $Ca^{2+}$ model in our study was adapted from Politi and colleagues (Politi et al., 2006). The model
191 equations and the descriptions of the parameters are shown in Figure 1 D, E and Table S1. We

192 modified the rate of $IP_3R$ inactivation term, $r$, to replicate our experimental $Ca^{2+}$ dynamics. The
193 modified equation is described below:

194 $$\frac{dr}{dt} = \frac{1}{\tau_{max}} \frac{k_\tau^4 + c^4}{k_\tau^4} (1 - r \frac{K_i + c}{K_i})$$

195 A similar modification to the rate of inactivation term, $r$, has been proposed previously (Sneyd et
196 al., 2017).

197 To reproduce the four distinct patterns in silico, we varied the $V_{PLC}$ parameter progressively
198 in individual cells across a range of parameters (Table S1). Given that our patterns were
199 dependent on the concentration of FEX, we varied $V_{PLC}$ as a lumped-parameter representing the
200 level of agonist stimulation. The computational model successfully reproduced the four different
201 spatiotemporal classes of $Ca^{2+}$ signaling dynamics observed in vivo and ex vivo (Figure 2A-D, SI
202 videos 9-12). Interestingly, we discovered that the formation of these patterns is dependent on
203 the number of cells having a $V_{PLC}$ value below, above, or equal to the Hopf bifurcation threshold
204 for single-cells ($V_{PLC}$ = 0.774) (Figure 2E). Simulated cells that have a $V_{PLC}$ value above the Hopf
205 threshold are termed "initiator cells" and are posed to exhibit high levels of $IP_3$ production.
206 Neighboring simulated cells with $V_{PLC}$ values below the Hopf threshold are termed "standby cells"
207 that receive a signal from initiator cells to propagate a signal. For instance, if a majority of standby
208 cells have $V_{PLC}$ values significantly below the critical Hopf bifurcation threshold, single-cell $Ca^{2+}$
209 spikes occur only where initiator cells are present (Figure 2A, E). When we increased standby
210 cell $V_{PLC}$ values close to the lower end of the Hopf bifurcation point (Figure 2B, E), we noticed the
211 formation of ICTs. Finally, we observed the formation of ICWs and fluttering phenotypes (Figure
212 2C, D, E) for cases when the majority of cells in the system were assigned a $V_{PLC}$ above the
213 bifurcation threshold, thereby placing most cells in an initiator state. In the absence of initiator
214 cells, $Ca^{2+}$ activity is not observed. This suggests that initiator cells are necessary for the formation
215 of $Ca^{2+}$ transients in developing tissues.

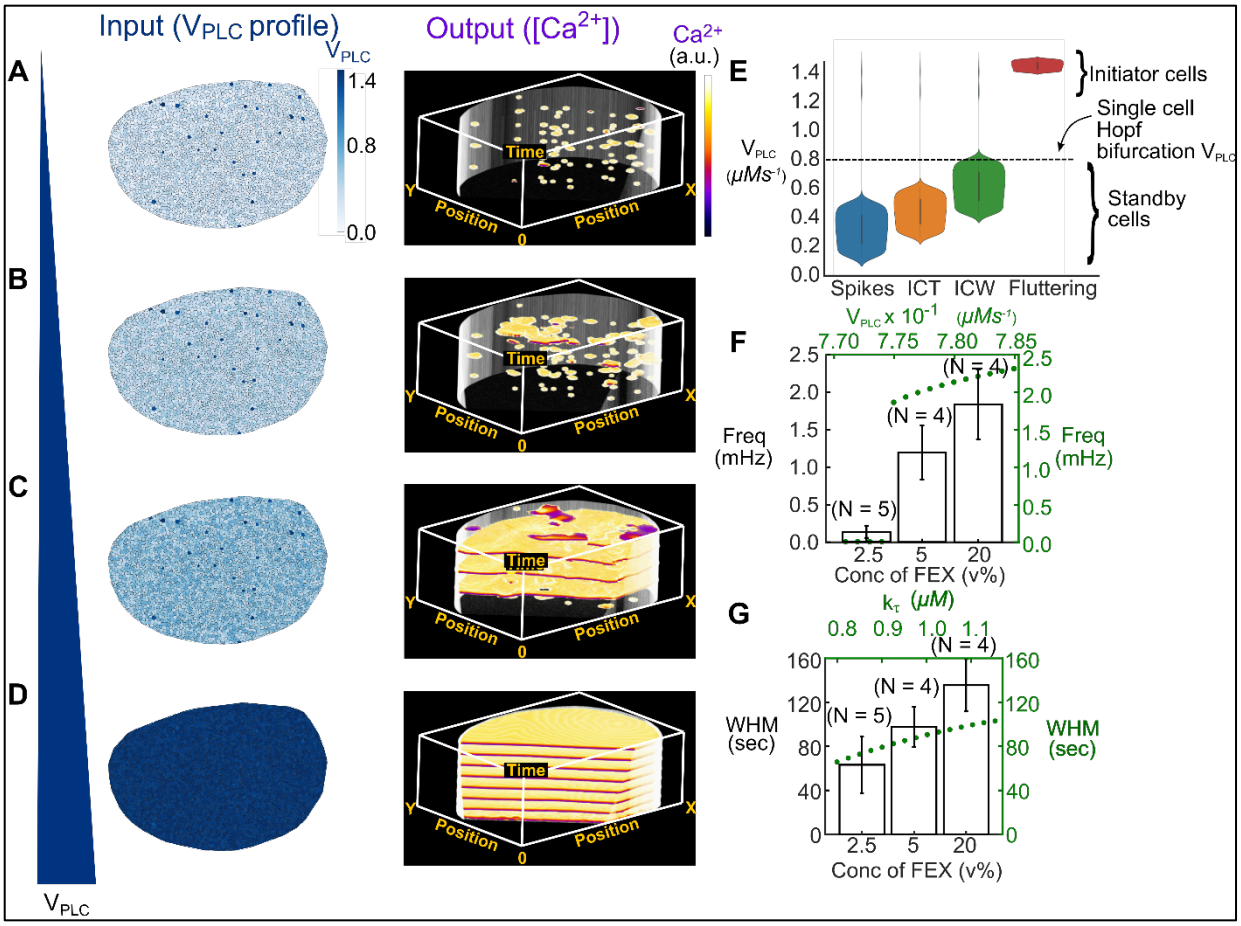


**Figure 2: A progression of hormonal stimulation governs the spatial extent of intercellular $Ca^{2+}$ communication. (A-D)** Computer simulations recapitulating the key classes of multicellular $Ca^{2+}$ activity observed in vivo and ex vivo. **(A)** When the majority of cells have $V_{PLC}$ values below the Hopf bifurcation threshold (*left*), single-cell $Ca^{2+}$ spikes are seen (*right*). **(B)** Intercellular $Ca^{2+}$ transients are observed (*right*) as the distribution of $V_{PLC}$ in cells is increased (*left*). **(C)** A further increase in $V_{PLC}$ (*left*) results in the emergence of periodic intercellular $Ca^{2+}$ waves (*right*). **(D)** "Fluttering" occurs (*right*) when $V_{PLC}$ levels in all of the cells in the disc is above Hopf bifurcation (*left*). **(E)** Quantification of $V_{PLC}$ distribution in the initiator and the standby cells for each of the classes of $Ca^{2+}$ signaling activity. The dashed line indicates the region in $V_{PLC}$ parameter space permitting $Ca^{2+}$ oscillations. **(F-G)** The single-cell version of our model predicts that the frequency and width at half maximum (WHM) of $Ca^{2+}$ oscillations is altered by varying $V_{PLC}$ and $k_\tau$. This prediction matches the WHM of $Ca^{2+}$ activity observed in ex vivo discs cultured with variable concentrations of fly extract. Error bars are reported as standard error of the means (SEM).

The "single-cell" version of the model predicts that differences in $Ca^{2+}$ signal amplitude and frequency are tunable by varying the $V_{PLC}$ and $k_\tau$ parameters (Figure S2 A,B). To further examine the influence of these and other parameters on $Ca^{2+}$ signaling dynamics, two-dimensional computational model simulations of the tissue were performed by varying $V_{PLC}$, $k_\tau$ and $\tau_{max}$ (Figure S3B-D) as a percentage of the baseline signal while holding other parameters constant. The

234 baseline parameter set was selected such that the simulation resulted in intercellular $Ca^{2+}$ waves
235 (Figure S3, red box). Reducing $k_\tau$ leads to a narrower width at half maximum (WHM) of $Ca^{2+}$
236 transients (Figure S3B). A similar result is observed when a reduction of $\tau_{max}$ results in a
237 decrease in WHM, whereas an increase in $\tau_{max}$ results in an increase in WHM (Figure S3C). A
238 decrease in the $\tau_{max}$ parameter increases the frequency of signals in the simulated tissue, while
239 an increase reduces the frequency of $Ca^{2+}$ transients. This suggests that the system is more
240 sensitive to $\tau_{max}$, and variations in $\tau_{max}$ have much greater impact in how quickly the system
241 responds to stimulus.

242 These results indicate that tissue-level $Ca^{2+}$ patterns depend on the spatial distribution of
243 cell states defined by their maximal $IP_3$ production rates, in relation to the effective tissue-level
244 Hopf bifurcation threshold. Further, key parameters in the model can be modified in a manner to
245 allow tunable $Ca^{2+}$ signaling patterns to influence signal strength, duration, and propagation.
246

247 **GJ communication limits $Ca^{2+}$ spikes in the absence of hormonal stimulation**

248 To elucidate how gap junctional proteins alter $Ca^{2+}$ signals, we simulated a scenario where
249 the initiator cells chosen at random had their $V_{PLC}$ values set to the Hopf bifurcation threshold
250 value of 0.774 and standby cells had a $V_{PLC}$ values that were randomly uniformly distributed
251 between 0.1 and 0.5 (Figure 3A). Under these conditions, no $Ca^{2+}$ activity was observed in the
252 presence of normal functioning GJ communication (Figure 3A'). Next, we compared the effect of
253 blocking gap junctional communication in silico. To do so, we set the permeability terms for $Ca^{2+}$
254 ($F_c$) and for $IP_3$ ($F_p$) to zero. Strikingly, we observed $Ca^{2+}$ spikes in simulated wing disc cells in the
255 absence of GJ communication (Figure 3A''). We explored this phenomenon computationally by
256 considering a single stimulated cell connected to neighboring cells by GJ communication by
257 performing bifurcation analysis on our modified model for a single-cell. We observed the
258 emergence of a Hopf bifurcation as expected (Figure S4A). Next, the effect of the initial Hopf
259 bifurcation point ($HB_1$) on gap junctional permeability of $IP_3$, $F_p$, was analyzed. Setting $F_c$ to zero

and progressively increasing $F_p$ increased the critical maximum rate of $IP_3$ activation threshold $V^*_{PLC}$ where $HB_1$ occurred (Figure S4B). Similar trends were observed when $F_c$ was increased to 0.05.

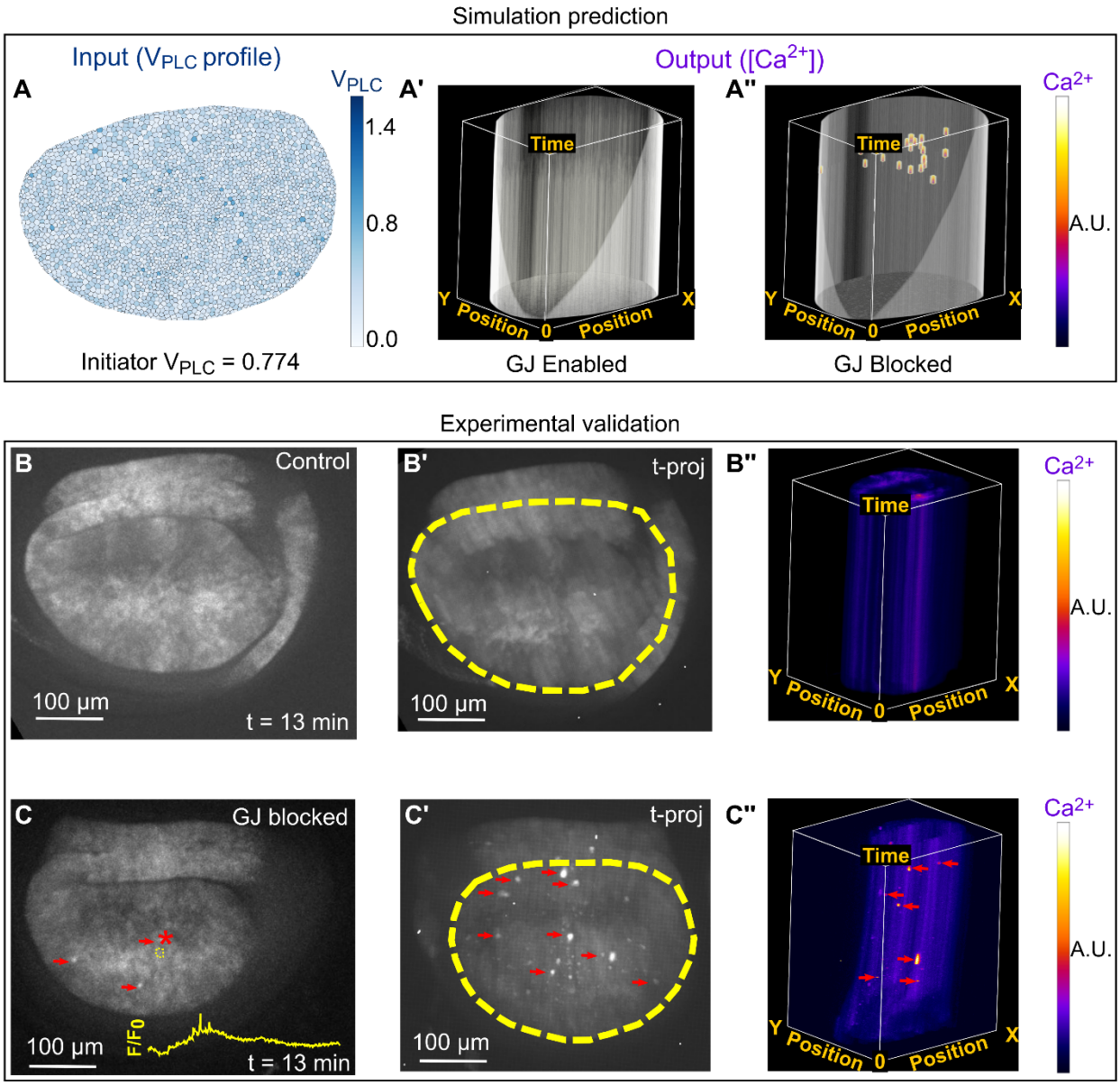


**Figure 3: Gap junction (GJ) communication decreases the proportion of cells exhibiting $Ca^{2+}$ spikes. (A)** Simulation of $Ca^{2+}$ signaling in wing disc where the $V_{PLC}$ values of initiator cells were set to the Hopf bifurcation threshold 0.774, and standby cell $V_{PLC}$ values were randomly distributed between 0.1 and 0.5. **(A')** Allowing GJ communication by letting permeability of $IP_3$ ($F_p$) and $Ca^{2+}$ ($F_c$ ) be 0.005 and 0.0005 respectively, resulted in no $Ca^{2+}$ activity (GJ Enabled). $F_p$ and $F_c$ were set to zero to simulate inhibition of GJ communication (GJ Blocked). Inhibition of GJ communication resulted in $Ca^{2+}$ spike activity. **(B)** Ex vivo time lapses of nub>GCaMP6f x UAS-$RyR^{RNAi}$ (control) wing discs in Grace's low ecdysone media were generated by imaging for 1 h at 10 sec intervals. Under this condition, we observed no $Ca^{2+}$ activity in the

wing disc cells. **(B')** Time-projection of the time lapse stack. The wing disc boundary is indicated with the yellow dashed line. **(B'')** A kymograph generated further demonstrates no instances of $Ca^{2+}$ activity. **(C)** GJ communication was blocked by culturing wing discs in Grace's low ecdysone media with 100 mM of Carbenoxolone (CBX). Instances of spike activity are denoted by red arrows. The intensity of a region of interest (yellow dashed circle) is overlaid to demonstrate a spike in local $Ca^{2+}$ activity. $Ca^{2+}$ spike is observed when the intensity normalized to basal intensity is plotted (yellow line, $F/F_0$). **(C')** Time-projection of the time lapse movies. We observed a significant number of $Ca^{2+}$ spikes in the 1 h time interval when GJs were inhibited. Yellow dashed lines indicated disc boundary**. (C'')** A kymograph generated demonstrates instances of $Ca^{2+}$ spike activity.

A closer look into the importance of GJ permeability on the formation of $Ca^{2+}$ signals was done by varying $F_c$ and $F_p$ in computational simulations. Starting from a baseline ICW, a decrease in GJ permeability resulted in a transition from ICWs to ICTs, and eventually to single-cell $Ca^{2+}$ spikes, while an increase in GJ permeability did not perturb the baseline signal (Figure S3A). These findings show that gap junctional permeability alters the cytosolic residence time for critical messengers such as $IP_3$ and $Ca^{2+}$ whose cytosolic concentrations affects $Ca^{2+}$ release from ER in both initiator cells and standby cells. This is consistent with bifurcation analysis demonstrating that gap junctional permeability influences stimulation threshold required for $Ca^{2+}$ oscillations in cells (Figure S4B).

We tested these computational modeling predictions experimentally. To do so, we pharmacologically inhibited the gap junctional protein Inx2 using Carbenoxolone (CBX) and observed the emergence of $Ca^{2+}$ spikes in the absence of FEX in the culture media (Figure 3B-B'', C-C'', SI movies 13,14). This further demonstrates that gap junction communication regulates $Ca^{2+}$ dynamics in the wing disc pouch.

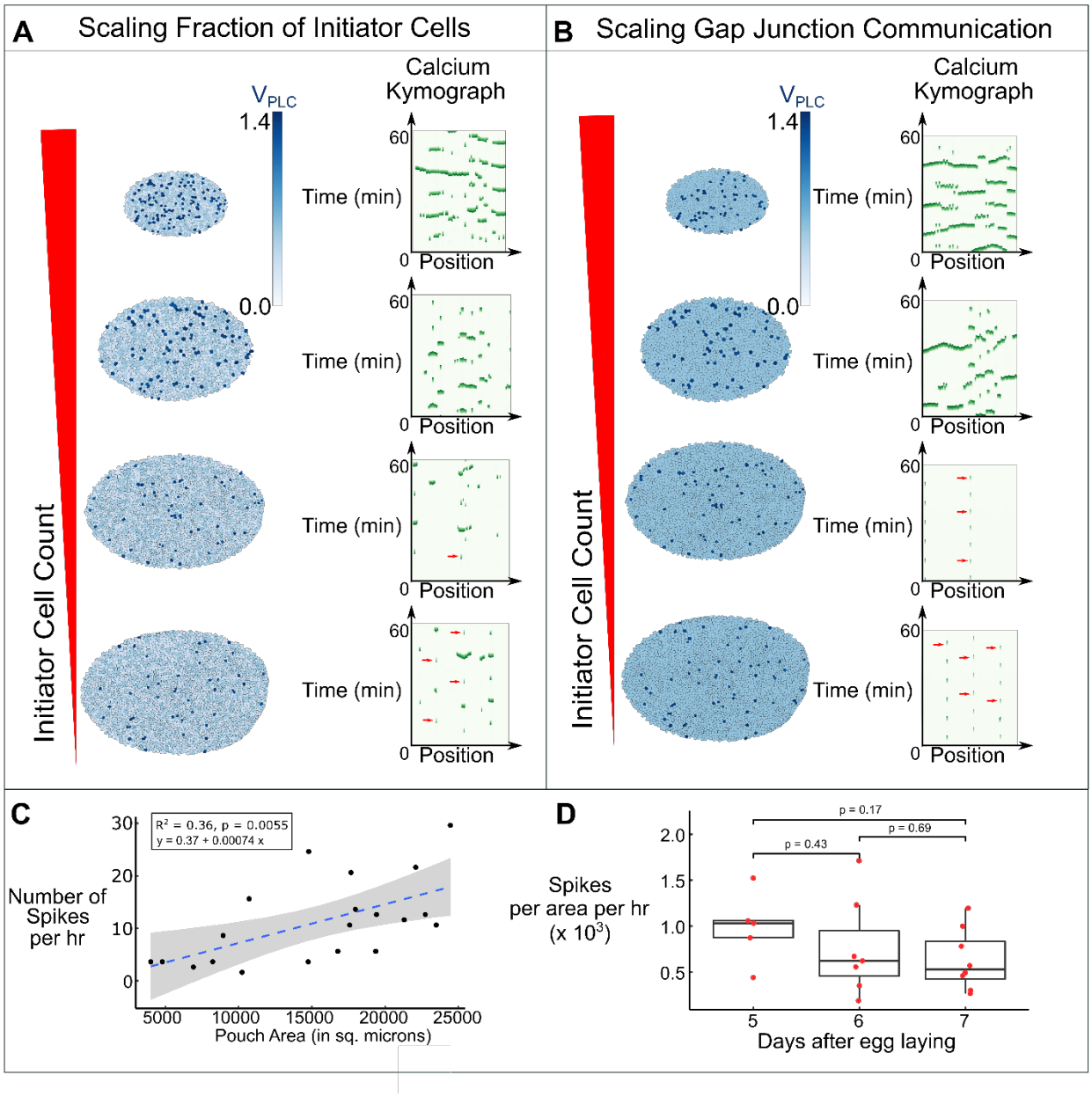


**Figure 4: Gap junctional permeability determines total tissue-level signaling activity as development progresses**. **(A-B)** Simulations of $Ca^{2+}$ signaling for wing discs of increasing size. In **A**, *(Left column)*, the fraction of initiator cells was varied according to the following equation: $Fraction\ of\ initator\ cells = 29{,}451 \cdot N_{cells}^{-1.8}$. The $V_{PLC}$ range of standby cells was restricted to range from 0.25 – 0.6 with initiator cells being denoted by dark blue cells with $V_{PLC}$ values between 1.3 and 1.5. *(Right column)* Associated 2D kymographs of the simulated pouches shown in **A**. In **B** *(Left column)*, the gap junction permeability is varied holding the fraction of initiator cell constant. Gap junction permeability was varied according to the following equation: $F_p = 1000 \cdot N_{cells}^{-1.8}$ and $F_c = 0.1 \cdot F_p$. The total number of initiator cells were held constant in this scenario ($N_{initiator} = 65$). *(Right column)* Associated kymographs of the simulated pouches. **(C-D)** Experimental validation of the computational predictions in which the discs were cultured ex vivo in Grace's low 20E media (basal media) for 1 h in the absence of any stimulus triggering $Ca^{2+}$. **(C)** Quantification of total number of $Ca^{2+}$ spikes in different sized wing disc pouch during 1 h culture. A linear regression line was fit to the data set and the p-value for the slope of the fitted line is shown. Since

309 the *p*-value is less than 0.05 (level of significance), a positive correlation between size and the number of
310 spikes could be inferred. Grey region corresponds to 95% confidence bands of the trend line. **(D)**
311 Quantification of total number of spikes in disc pouch scaled with respect to pouch size during various
312 stages of larval development. *p*-values were obtained by Mann Whitney U test.

313

314 **Gap junction permeability shapes $Ca^{2+}$ signaling during development**

315 Of note, integrated intensity of $Ca^{2+}$ throughout the wing disc pouch decreases during
316 development suggesting an inverse relationship between calcium activity and organ growth rates
317 (Brodskiy et al., 2019). Here, we investigated the role of tissue size in altering $Ca^{2+}$ dynamics to
318 propose an explanation for this finding. To do so, we simulated $Ca^{2+}$ signaling in different sized
319 wing discs. We hypothesized two different possible scenarios that could explain a decrease in
320 integrated $Ca^{2+}$ activity. In the first scenario, the total fraction of initiator cells was allowed to
321 decrease in a power law fashion as development proceeds resulting in a decay in total calcium
322 signaling activity with a transition to predominantly single-cell spiking activity. In the second
323 scenario, gap junction permeability was set to decrease with increasing organ size. Simulations
324 corresponding to each scenario shows an orderly decrease in progression of $Ca^{2+}$ activity starting
325 from ICWs and intercellular transients in smaller simulated discs and decaying to intermittent
326 single-cell spikes in larger simulated discs (Figure 4A, B). This suggests that both scenarios
327 provide a possible explanation for the decrease in integrated $Ca^{2+}$ activity observed in wing discs
328 as development progresses.

329 To distinguish between these scenarios, we cultured wing discs from multiple
330 developmental stages from days 5-7 after egg laying (AEL) without any agonist stimulation and
331 observed the resulting $Ca^{2+}$ dynamics. We observed single-cell $Ca^{2+}$ spikes that we interpret as
332 characteristic of "initiator" cells in all samples independent of sizes. We did not observe $Ca^{2+}$
333 transients or waves in unstimulated smaller wing discs obtained day 5 AEL. We next
334 characterized the total number of spikes in the discs of all sizes. We found a positive correlation
335 between the total number of spikes and the size of the disc pouch (Figure 4C). The difference in

336 spiking activity between discs of varying ages was not significant when scaled for pouch size
337 (Figure 4D). This is consistent with a scenario of a relatively constant number of initiator cells in
338 the system with overall gap junction permeability decreasing as the organ reaches its terminal
339 size. This scenario is further supported by findings from previous reports showing a decrease in
340 gap junctional permeability as larval development proceeds (Weir and Lo, 1982, 1985).
341 Furthermore, a decrease in gap junction permeability increases the net cytosolic residence time
342 and effective concentrations of $IP_3$ and $Ca^{2+}$ within the cytosol leading to an increased instance
343 of cytosolic $Ca^{2+}$ spikes.

344 **Gαq overexpression induces intercellular $Ca^{2+}$ waves and reduces wing size**

345 Next, using the GAL4/UAS system, we overexpressed the wild type splice 3 variant of
346 *Drosophila* Gαq in the wing disc to characterize how different classes of upstream signals impact
347 the spatiotemporal patterns of $Ca^{2+}$ signaling (Ratnaparkhi et al., 2002). G protein-coupled
348 receptor (GPCR) activation stimulates Gαq-driven PLC$\beta$ activity to generate $IP_3$ and $Ca^{2+}$ (Hanlon
349 and Andrew, 2015). Strikingly, ectopic Gαq expression was sufficient to generate robust formation
350 of intercellular waves independent of the presence of FEX in the media (Figure 4D, D'). The waves
351 were periodic in nature and were similar to FEX-induced waves (Figure 1C). This experimental
352 finding most likely resembles our previous simulation of ICWs with a small fraction of randomly
353 located initiator cells surrounded by standby cells (Figure 2C).

354 Strikingly, the wing disc size (day 6 AEL) and adult wing size were significantly reduced
355 when Gαq was overexpressed (Figure 4E-F). To understand whether the reduction in the wing
356 size was due to changes in proliferation or cell growth, we quantified the total number of cells in
357 the region bounded by the LIII, LIV, ACV wing veins and the wing margin. We observed a
358 reduction in the total number of trichomes, which each individual trichome correspond to a cell
359 (García-Bellido et al., 1994). Furthermore, we found that cell size was reduced when Gαq was
360 overexpressed (Figure S5F). However, the wing shape is not significantly affected when Gαq is

361 overexpressed (Figure S5G). In sum, increasing the concentration of Gαq in the pouch is sufficient
362 to generate periodic $Ca^{2+}$ waves. Further, these periodic $Ca^{2+}$ waves are correlated with reduction
363 in wing and disc size suggesting that tissue-wide $Ca^{2+}$ wave activity may play a role in determining
364 final organ size via growth inhibition.

365 **Insulin signaling increases wing size but only generates localized $Ca^{2+}$ signals**

366 Because FEX is an undefined cocktail of biochemical factors, we tested whether specific
367 ligands added to the organ culture affects $Ca^{2+}$ activity and growth. In addition to FEX, insulin is
368 often added to organ culture media to stimulate cell proliferation (Wyss, 1982; Zartman et al.,
369 2013). Hence, we tested whether insulin signaling regulates $Ca^{2+}$ activity independent of FEX.
370 Similar to other experiments, we upregulated and downregulated insulin signaling in the wing disc
371 using the GAL4/UAS expression system. As expected, wing disc size and adult wing size were
372 decreased when insulin signaling is downregulated (Figure 4B, E, F). Strikingly, we observed that
373 activation of insulin stimulated pathways results in localized $Ca^{2+}$ spikes and ICTs (Figure 4B, B',
374 C, C'). Titrated the concentration of insulin in the culture media demonstrated that a higher
375 concentration of insulin increased the number of spikes (Figure 4G). Quantification of the $Ca^{2+}$
376 spikes showed a positive correlation between spikes normalized to area of the pouch with log of
377 insulin concentration (Fig 4G). However, even high concentrations of insulin were not sufficient to
378 generate periodic ICWs. In contrast, expressing a dominant negative form of the insulin receptor
379 resulted in minimal $Ca^{2+}$ spiking activity (Figure 4C, C') (Hevia et al., 2017). These results
380 demonstrate that insulin signaling stimulates $Ca^{2+}$ activity in the wing disc.

381 In silico simulations with parameter variations in half activation of the PLC parameter, $K_{PLC}$,
382 and GJ permeability were performed to test scenarios of how insulin signaling can only generate
383 $Ca^{2+}$ spiking activity even under saturating conditions (Figure S3A, S3D, and S6). Although $K_{PLC}$
384 variations influenced signal frequency, there was no instance in which varying $K_{PLC}$ resulted in
385 production of $Ca^{2+}$ spikes. Single-cell spikes were only observed when gap junction

386 communication was inhibited either experimentally (Figure 3B, C) or in silico (Figure 3A, Figure
387 S3A). Thus, the computational model suggests that insulin signaling must not only stimulate $IP_3$
388 production, but also inhibits gap junction permeability.

389 As a first step to assess whether $Ca^{2+}$ levels in the cell directly control organ sizes, we
390 exploited the $Ca^{2+}$ buffering effects induced by high levels of GCaMP6f sensor expression. The
391 GCaMP6f sensor consists of a M13 fragment of myosin light chain kinase, GFP and Calmodulin
392 (CaM) to which $Ca^{2+}$ binds (Nakai et al., 2001). To elucidate the role of $Ca^{2+}$ signaling in insulin
393 mediated growth, we compared the effects of co-expressing the GCaMP6f sensor ($K_d = 375 \pm$
394 $14\, nM$) to decrease the amount of free cytosolic $Ca^{2+}$ (Chen et al., 2013). We found that co-
395 expressing GCaMP6f sensor increased wing size when insulin signaling was also stimulated
396 (Figure S7). This increase in size was also observed in control wing disc without insulin
397 upregulation (Figure S7A, B). This analysis provides additional evidence that buffering cytosolic
398 $Ca^{2+}$ signaling influences the final tissue size. In contrast, when we expressed Gαq and GCaMP6f,
399 we did not observe a significant decrease in size when compared to just expressed Gαq without
400 GCaMP6f (Figure S7 C, D). This may be due to the inability of GCaMP6f expression to buffer the
401 high levels of $Ca^{2+}$ in the cytosol when Gαq is overexpressed. We also observed a severe
402 reduction in the wing size, along with vein defects, in flies that were homozygous for the GCaMP6f
403 sensor, consistent with a buffering role for high concentrations of GCaMP6f expression (Figure
404 S8). To validate this finding, we compared the adult wing sizes from flies expressed one and two
405 copies of GCaMP6f. Strikingly, increasing the dose of the relative GCaM6f expression decreased
406 the size (Figure S8 C, D). We observed a severe reduction in size as expression of the transgene
407 was further increased with the presence of two copies of the GAL4 driver. To further elucidate the
408 sponging effects of $Ca^{2+}$, we expressed CaMKII, which binds to $Ca^{2+}$/CaM complex (Yamauchi,
409 2005). Similar to overexpressing GCaM6f, we observe a significant increase in the wing area
410 (Figure S8E, F). Collectively, these results support a role of cytosolic $Ca^{2+}$ concentration as either
411 a growth enhancer or suppressor and that an optimal amount of $Ca^{2+}$ signaling is required for

robust size control.

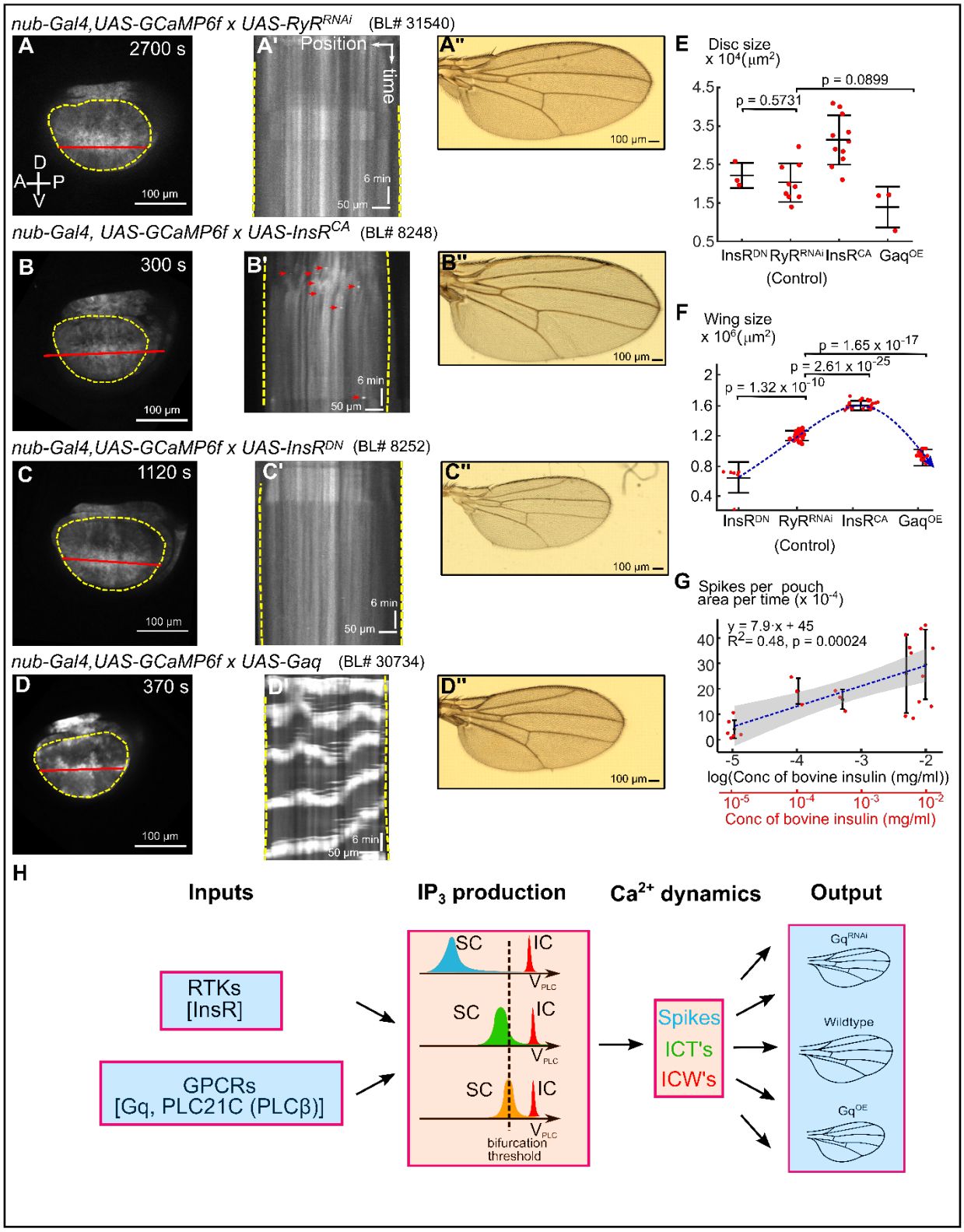

414 **Figure 5: GPCR and insulin signaling regulate wing size and differentially regulate $Ca^{2+}$ signaling.**
415 **(A-D)** Montages of time-lapse movies of wing discs cultured ex vivo. **(A'-D')** Kymographs of the
416 corresponding time-lapse movies. **(A"-D")** Adult wings from the indicated genetic perturbation. **(E)**
417 Quantification of the wing disc sizes for the indicated genetic perturbations. **(F)** Quantification of the adult
418 wing sizes for the indicated perturbations. **(G)** Quantification of $Ca^{2+}$ spikes when insulin dose is
419 progressively increased in ex vivo cultures. A linear regression trend line was fit to the data and the *p*-value
420 of the slope is shown. Since the *p*-value is less than 0.05, a positive correlation between spikes and the
421 log(concentration) can be inferred. Grey region illustrates 95% confidence bands of the linear regression
422 **(I)** Summary of key findings based on the proposed model for tissue-level regulation of dynamics in
423 epithelial tissues. Scale bars in (A-D) and (A"-D") represent 100 μm, while yellow dotted lines indicate pouch
424 boundaries, and red lines indicate x-y positions in the kymograph. Horizontal scale bars in (A'-D') represent
425 50 μm. Vertical scale bars in (A'-D') represent 6 min. Student t-test was performed. Labels in (E) represent
426 crosses of UAS-transgene to parental nub>GCaMP6f in the case of $InsR^{CA}$ and $InsR^{DN}$ or nub>GCaMP6f;
427 mcherry in the case of $RyR^{RNAi}$ or Gαq. The UAS lines used are UAS-$RyR^{RNAi}$ (BL#31540), UAS $InsR^{CA}$
428 (BL#8248), UAS-$InsR^{DN}$ (BL#8252) and UAS-Gq (BL#30734) respectively.

429 **Discussion**

430 The main finding of this work is the discovery of a parsimonious mechanistic model that
431 links global hormonal stimulation of $Ca^{2+}$ signaling to emergent spatiotemporal classes of
432 signaling dynamics. Further, we identify downstream correlations to the final organ size that
433 suggest these signaling dynamics may mediate growth-related information used by the system to
434 tune organ size. To do so, we developed a geometrically accurate computational model of $Ca^{2+}$
435 signaling in the *Drosophila* wing imaginal disc, a premier model for studying conserved cell
436 signaling mechanisms (Hariharan, 2015; Johnston and Gallant, 2002; Potter, 2001). Previously,
437 we discovered a correlation between $Ca^{2+}$ signaling during larval growth and final organ size. Four
438 distinct patterns of $Ca^{2+}$ signaling activity occur in the wing imaginal disc pouch as observed in
439 vivo and ex vivo (Brodskiy et al., 2019). Through systems-level computational analysis, we
440 established the essential conditions required for generating the different patterns.

441 The model predicts two cell types with different levels of $IP_3$ production: "initiator cells" with
442 high $IP_3$ production and "standby cells" with baseline $IP_3$ production levels. The presence of
443 initiator cells is necessary, but not sufficient, to induce multicellular $Ca^{2+}$ signaling. Additionally,
444 the distribution of the maximal rate of $IP_3$ production, $V_{PLC}$, in the standby cells determines the
445 spatial range of $Ca^{2+}$ signaling. As $V_{PLC}$ values of standby cells approaches the Hopf bifurcation
446 threshold, $Ca^{2+}$ activity transitions from single-cell signals toward global signals.

What are the possible functional implications of a tissue consisting of initiator and standby cells? A recent study on electrical signal transmission in bacterial communities suggests that the transition from localized short-range signaling to global community-level communication is associated with a cost-benefit balance (Larkin et al., 2018). In that context, long-range signaling increases the overall fitness of the community against chemical attacks, while a reduction in growth rate is the cost to individual cells. In the wing disc, a similar analogy can be drawn where significant generation of long-range $Ca^{2+}$ signals due to overexpression of Gαq results in reduced wing disc growth. Thus, the proposed model in this work can also be characterized as a cost-benefit tradeoff within the context of tissue-level signaling. For instance, it has been suggested that the fast $Ca^{2+}$ waves facilitate migration and proliferation of the healing cells by inhibiting excessive apoptotic response during wound healing in epithelia (Justet et al., 2016).

Our model also predicts that the inhibition of GJs lowers the Hopf threshold necessary for generating $Ca^{2+}$ spikes. We have validated this prediction experimentally where inhibition of GJs results in the formation of $Ca^{2+}$ spikes in the absence of external agonist. Further, computational simulations demonstrate that as GJ permeability decreases, there is a transition of activity from synchronous global to asynchronous local $Ca^{2+}$ activity. How gap junctional mediated $Ca^{2+}$ signaling is connected to the regulation of cell mechanics is not currently understood and warrants further investigation. One possibility is that tension impacts the level of gap junction communication between cell and may also influence the activity of mechanosensitive ion channels (Kaouri et al., 2019). Feedback between calcium signaling and cell mechanics may play important roles in ensuring tissue growth and morphogenesis. This is evident from our previous experimental work and other experimental studies in the literature where knockdown of gap junctional proteins such as Inx2 leads to a reduction in wing and eye size in *Drosophila* (Brodskiy et al., 2019; Richard et al., 2017).

471 Upregulated insulin signaling increases the formation of $Ca^{2+}$ spikes. One possible
472 implication is that insulin signaling inhibits GJs in addition to increasing PLC$\gamma$ activity. This
473 implication is consistent with the role of insulin signaling in inhibiting gap junction proteins
474 Connexin43 (Homma Nobuo et al., 1998; Lin et al., 2003; Warn-Cramer and Lau, 2004). Thus,
475 the increase of adult wing and developing wing disc size from higher insulin activity correlates
476 with higher levels of localized $Ca^{2+}$ spiking activity, which has a limited total integrated calcium
477 signal at that tissue level. In contrast, $Ca^{2+}$ waves induced by Gαq overexpression are correlated
478 with smaller adult wings and wing discs. Higher Gαq expression, which activates PLC$\beta$ activity
479 results in robust production of tissue-scale intercellular $Ca^{2+}$ waves. We show experimentally that
480 insulin signaling controls $Ca^{2+}$ spike activity in the wing disc, potentially through GJ inhibition or
481 PLC$\gamma$ activation, whereas GPCR-based Gαq signaling is sufficient to generate global $Ca^{2+}$ waves.
482 These results are consistent with previous reports of $Ca^{2+}$ spikes being observed in discs that
483 have reached their final size, and $Ca^{2+}$ waves being observed in smaller developing discs
484 (Brodskiy et al., 2019). A recent study reported after we archived this study as a preprint found
485 that $Ca^{2+}$ signals are initiated in response to wounding by the G-protein coupled receptor
486 Methuselah like 10 (Mthl10) (O'Connor et al., 2020). Mthl10 is activated by Growth-blocking
487 peptides (Gbps) (O'Connor et al., 2020). Whether Mthl10 also is involved in developmental growth
488 requires further investigation, but may be consistent with our findings that intercellular calcium
489 wave activity inhibit organ growth. These findings suggest that $Ca^{2+}$ acts as both a growth
490 enhancing and growth inhibiting signal dependent upon the tissue-level scale of the activity and
491 level of gap junction coupling.

492 The spatial range of tissue-level signaling is determined by how the $IP_3$ production is
493 organized with respect to a Hopf bifurcation threshold throughout the tissue. Localized transients
494 are correlated with larger wings induced by insulin-stimulated growth. Global signaling is
495 correlated with smaller wings that are stimulated by upstream GPCRs and Gαq upregulation. This
496 resembles a paradoxical network motif where the $Ca^{2+}$ signaling has two opposite effects on the

497 same target, dependent upon the tissue-level scale of the $Ca^{2+}$ signal. Within the context of the
498 hypothesized $IP_3$/shunt model proposed in our previous study, the strong induction of $Ca^{2+}$ waves
499 will reduce the level of phosphatidylinositol 4,5-bisphosphate ($PIP_2$), a key substrate for growth
500 (Brodskiy et al., 2019). This may occur as high levels of Gαq/PLC activity are proposed to deplete
501 $PIP_2$ levels (Loew, 2007). This is likely due to substrate depletion of $PIP_2$ through promotion of $IP_3$
502 generation and downstream activity by stimulation of PLC activity. In turn, this would lead to
503 reduced availability of $PIP_2$ for conversion of $PIP_2$ to phosphatidylinositol-trisphosphate ($PIP_3$), a
504 key second messenger for stimulating protein kinase AKT and downstream growth promotion
505 (Czech, 2000).

506 Similar to the reduced wing size observed in this study due to overexpression of Gαq, we
507 have also reported that knockdown of Gαq gene decreases wing size in our previous study (Table
508 S3) (Brodskiy et al., 2019). Comparing the reduction in wing size due to perturbation of $Ca^{2+}$
509 signaling components with known size control genes such as morphogens (Dpp, Wg, Hippo) and
510 mechanical transducers (RoK) indicate that the reduction in size is comparable to when $Ca^{2+}$
511 signaling is perturbed (Table S3). Taken together, these experimental findings imply that Gαq
512 signaling is paradoxical in nature. In the context of conserved network motif observed in biological
513 systems, paradoxical components have the ability to activate and inhibit the downstream target
514 despite a single source of stimulus (Hart and Alon, 2013). Gαq could possibly be a growth
515 promoter and growth inhibitor. This correlation motivates further studies that map out the exact
516 molecular players that are downstream of Gαq signaling. This will require careful quantification of
517 $PIP_2$ and $PIP_3$ under genetic perturbations of GPCR signaling. Additionally, future work is needed
518 to quantify the metabolic benefits and costs of $Ca^{2+}$ signaling during tissue growth to observe if
519 abundant use of metabolic resources to consistently propagate global activity is explanatory for
520 the reduction in size in Gαq overexpression wings.

521

522

523 **Materials and Methods**

524 ***Drosophila genetics.***

525 We used the GAL4/UAS system to express modulators of the $Ca^{2+}$ signaling pathway in the wing
526 disc (Brand and Perrimon, 1993; Duffy, 2002). A nub-GAL4, UAS-GCaMP6f reporter tester line
527 was created by recombining nub-GAL4 and UAS-GCaMP6f lines (Narciso et al., 2015).
528 Additionally, a second tester line was used that also includes UAS-mcherry. Gene perturbations
529 were generated by crossing the tester line to either RNAi-based transgenic lines (UAS-Gene
530 $X^{RNAi}$) or gene overexpression (UAS-Gene X). The following UAS transgenic lines were used:
531 UAS-$RyR^{RNAi}$ (BL#31540) (Perkins et al., 2015), UAS-Gq (BL#30734) (Perkins et al., 2015), UAS-
532 $InsR^{CA}$ (BL#8248) (Werz et al., 2009), UAS-$InsR^{DN}$ (BL#8252) (Kakanj et al., 2016). Progeny wing
533 phenotypes are from F1 male progeny emerging form the nub-Gal4, UAS-GCaMP6f/CyO x UAS-
534 X cross or nub-Gal4, UAS-GCaMP6f/CyO; UAS-mcherry x UAS-X cross. Flies were raised at 25
535 °C and on a 12-hour light cycle.

536 ***Live imaging.***

537 Wandering third instar larva approximately 6 days after egg laying were dissected in ZB media
538 with 15% fly extract to obtain wing discs (Brodskiy et al., 2019). ZB media + 15% fly extract
539 contains 79.4% (v/v) ZB media, 0.6% (v/v) of 1 mg/ml of insulin (Sigma aldrich), 15% ZB-based
540 fly extract and 5% penicillin/streptomycin (Gibco). Wing discs were loaded into the previously
541 described REM-Chip (Narciso et al., 2017) and imaged using Nikon Eclipse Ti confocal
542 microscope with a Yokogawa spinning disc and MicroPoint laser ablation system. Image data
543 were collected on an IXonEM+colled CCD camera (Andor technology, South Windsor, CT) using
544 MetaMorph v7.7.9 software (Molecular devices, Sunnyvale, CA). Discs were imaged at three z-
545 planes with a step size of 10 μm, 20x magnification and 10-seconds intervals for a total period of
546 one hour, with 200 ms exposure time, and 50 nW, 488 nm laser exposure at 44 % laser intensity.
547 We blocked GJ by inhibiting innexin-2 using Carbenoxolone (Cbx, Sigma Aldrich) drug (Narciso
548 et al., 2015). Wing discs were incubated in ZB + 15% FEX with 30 μM Cbx for one hour before

549 imaging. To induce $Ca^{2+}$ transients, we imaged wing discs in ZB media + 2.5 % FEX (Burnette
550 et al., 2014) . $Ca^{2+}$ waves were induced by imaging the wing disc in ZB media + 15% FEX. $Ca^{2+}$
551 fluttering was observed when discs were imaged in ZB media + 40% FEX respectively.

552 ***Image processing***

553 All the images were processing in FIJI. Volume viewer plugin was used to generate 3D
554 Kymographs. Briefly, TIFF stacks had background subtracted using the rolling ball background
555 subtraction algorithm with a rolling ball radius of 15. The TIFF stack was then processed by the
556 volume viewer plugin. Stacks were adjusted using the base Fire LUT setting to portray the
557 signaling intensities. A similar approach was followed for the simulation outputs.

558 ***Model formulation.***

559 Figure 1 summarizes the experimental system and data. Different classes of patterns emerge at
560 the tissue-level as the level of global stimulation increases: spikes, intercellular $Ca^{2+}$ transients
561 (ICTs), intercellular $Ca^{2+}$ waves (ICWs) and global fluttering (Brodskiy et al., 2019). However, a
562 mechanistic understanding linking hormonal stimulation levels to transitions in these qualitative
563 classes of organ-level signaling is lacking. We therefore formulated a computational model to test
564 mechanistic hypotheses that could explain the observed $Ca^{2+}$ signaling dynamics.

565 ***Intracellular model.***

566 A modified model of $Ca^{2+}$ signaling toolkit is based on adaptation of previous single-cell model of
567 calcium signaling (Politi et al., 2006). The model is summarized in Figure 1E. A more
568 comprehensive description can be found in Supporting Information. To recapitulate the same time
569 resolution as the experiments, the simulation time is 1 hour and for generating videos, samples
570 are obtained every 10 s.

571 ***Tissue model.***

572 For constructing a realistic model of the tissue, we used experimental images of a wing pouch to
573 build an accurate model of the tissue structure. Figure S1 depicts the structure of the tissue used

for simulations and the statistics of the corresponding network. More details on the geometry of the model are discussed in Supporting Information.

***Multicellular model.***

The realistic model of the tissue was combined with proposed intracellular model. Diffusion of the second messengers $IP_3$ and $Ca^{2+}$ between adjacent cell was incorporated into the 2D model. Therefore, the tissue level model is a system of coupled ODE's. A complete description of the model is provided in Supporting Information.

## Quantification and Statistical Analysis

***Quantification of adult wings and statistics.***

Total wing area was measured using ImageJ. We traced the wing margin by following veins L1 and L5 and the wing hinge region was excluded from the size analysis. All statistical analyses were performed using MATLAB or R. For comparisons, we used student t-tests to assess the statistical significance. *p*-value, standard deviation and sample size (n) are as indicated in each figure and legend.

## Data and Code Availability

All the data and simulation codes are available on our lab GitHub repository: https://multicellularsystemslab.github.io/MSELab_Calcium_Cartography_2021/


## Acknowledgements

The work in this paper was supported by NIH Grant R35GM124935 and NSF Award CBET-1553826. The authors gratefully acknowledge the Notre Dame Center for Research Computing (CRC) for providing computational facilities. The authors would also like to thank members of the Zartman lab for helpful discussions.

## References


Balaji, R., Bielmeier, C., Harz, H., Bates, J., Stadler, C., Hildebrand, A., and Classen, A.-K. (2017). Calcium spikes, waves and oscillations in a large, patterned epithelial tissue. Scientific Reports *7*, 42786.

Berridge, M.J. (1987). Inositol Trisphosphate and Diacylglycerol: Two Interacting Second Messengers. Annual Review of Biochemistry *56*, 159–193.

Berridge, M.J. (2005). Unlocking the secrets of cell signaling. Annu. Rev. Physiol. *67*, 1–21.

Berridge, M.J., Lipp, P., and Bootman, M.D. (2000). The versatility and universality of calcium signalling. Nature Reviews Molecular Cell Biology *1*, 11.

Brand, A.H., and Perrimon, N. (1993). Targeted gene expression as a means of altering cell fates and generating dominant phenotypes. Development *118*, 401–415.

Brodskiy, P.A., Wu, Q., Soundarrajan, D.K., Huizar, F.J., Chen, J., Liang, P., Narciso, C., Levis, M.K., Arredondo-Walsh, N., Chen, D.Z., et al. (2019). Decoding calcium signaling dynamics during *Drosophila* wing disc development. Biophysical Journal *116*, 725–740.

Buchmann, A., Alber, M., and Zartman, J.J. (2014). Sizing it up: The mechanical feedback hypothesis of organ growth regulation. Seminars in Cell & Developmental Biology *35*, 73–81.

Burnette, M., Brito-Robinson, T., Li, J., and Zartman, J. (2014). An inverse small molecule screen to design a chemically defined medium supporting long-term growth of *Drosophila* cell lines. Molecular BioSystems *10*, 2713–2723.

Carafoli, E. (2002). Calcium signaling: a tale for all seasons. Proceedings of the National Academy of Sciences *99*, 1115–1122.

Ceriani, F., Pozzan, T., and Mammano, F. (2016). Critical role of ATP-induced ATP release for $Ca^{2+}$ signaling in nonsensory cell networks of the developing cochlea. Proceedings of the National Academy of Sciences *113*, E7194–E7201.

Chen, T.-W., Wardill, T.J., Sun, Y., Pulver, S.R., Renninger, S.L., Baohan, A., Schreiter, E.R., Kerr, R.A., Orger, M.B., Jayaraman, V., et al. (2013). Ultrasensitive fluorescent proteins for imaging neuronal activity. Nature *499*, 295–300.

Clapham, D.E. (2007). Calcium Signaling. Cell *131*, 1047–1058.

Cuthbertson, K.R., and Cobbold, P. (1985). Phorbol ester and sperm activate mouse oocytes by inducing sustained oscillations in cell $Ca^{2+}$. Nature *316*, 541.

Czech, M.P. (2000). PIP2 and PIP3: complex roles at the cell surface. Cell *100*, 603–606.

Duffy, J.B. (2002). GAL4 system in *Drosophila*: a fly geneticist's Swiss army knife. Genesis *34*, 1–15.

García-Bellido, A., Cortés, F., and Milán, M. (1994). Cell interactions in the control of size in *Drosophila* wings. Proc Natl Acad Sci U S A *91*, 10222–10226.

633 Giorgi, C., Danese, A., Missiroli, S., Patergnani, S., and Pinton, P. (2018). Calcium dynamics as
634 a machine for decoding signals. Trends in Cell Biology *28*, 258–273.

635 Gómez, H.F., Georgieva, L., Michos, O., and Iber, D. (2017). Image-Based In silico Models of
636 Organogenesis. In Systems Biology, (John Wiley & Sons, Ltd), pp. 319–340.

637 Gou, J., Stotsky, J.A., and Othmer, H.G. (2020). Growth control in the *Drosophila* wing disk.
638 WIREs Systems Biology and Medicine *12*, e1478.

639 Hanlon, C.D., and Andrew, D.J. (2015). Outside-in signaling – a brief review of GPCR signaling
640 with a focus on the *Drosophila* GPCR family. J Cell Sci *128*, 3533–3542.

641 Hariharan, I.K. (2015). Organ Size Control: Lessons from *Drosophila*. Developmental Cell *34*,
642 255–265.

643 Hart, Y., and Alon, U. (2013). The Utility of Paradoxical Components in Biological Circuits.
644 Molecular Cell *49*, 213–221.

645 Hevia, C.F., López-Varea, A., Esteban, N., and de Celis, J.F. (2017). A Search for Genes
646 Mediating the Growth-Promoting Function of TGFβ in the *Drosophila melanogaster* Wing Disc.
647 Genetics *206*, 231–249.

648 Homma Nobuo, Alvarado José Luis, Coombs Wanda, Stergiopoulos Kathleen, Taffet Steven M.,
649 Lau Alan F., and Delmar Mario (1998). A Particle-Receptor Model for the Insulin-Induced
650 Closure of Connexin43 Channels. Circulation Research *83*, 27–32.

651 Humeau, J., Bravo-San Pedro, J.M., Vitale, I., Nuñez, L., Villalobos, C., Kroemer, G., and
652 Senovilla, L. (2017). Calcium signaling and cell cycle: progression or death. Cell Calcium.

653 Johnston, L.A., and Gallant, P. (2002). Control of growth and organ size in *Drosophila*.
654 BioEssays *24*, 54–64.

655 Jursnich, V.A., Fraser, S.E., Held, L.I., Ryerse, J., and Bryant, P.J. (1990). Defective gap-
656 junctional communication associated with imaginal disc overgrowth and degeneration caused by
657 mutations of the dco gene in *Drosophila*. Developmental Biology *140*, 413–429.

658 Justet, C., Hernández, J.A., Torriglia, A., and Chifflet, S. (2016). Fast calcium wave inhibits
659 excessive apoptosis during epithelial wound healing. Cell and Tissue Research *365*, 343–356.

660 Kakanj, P., Moussian, B., Grönke, S., Bustos, V., Eming, S.A., Partridge, L., and Leptin, M.
661 (2016). Insulin and TOR signal in parallel through FOXO and S6K to promote epithelial wound
662 healing. Nature Communications *7*, 12972.

663 Kaouri, K., Maini, P.K., Skourides, P.A., Christodoulou, N., and Chapman, S.J. (2019). A simple
664 mechanochemical model for calcium signalling in embryonic epithelial cells. Journal of
665 Mathematical Biology.

666 La Rovere, R.M., Roest, G., Bultynck, G., and Parys, J.B. (2016). Intracellular $Ca^{2+}$ signaling
667 and $Ca^{2+}$ microdomains in the control of cell survival, apoptosis and autophagy. Cell Calcium
668 *60*, 74–87.

669 Larkin, J.W., Zhai, X., Kikuchi, K., Redford, S.E., Prindle, A., Liu, J., Greenfield, S., Walczak,
670 A.M., Garcia-Ojalvo, J., Mugler, A., et al. (2018). Signal Percolation within a Bacterial
671 Community. Cell Systems *7*, 137–145.

672 Leptin, M. (1995). *Drosophila* Gastrulation: From Pattern Formation to Morphogenesis. Annual
673 Review of Cell and Developmental Biology *11*, 189–212.

674 Levin, M. (2007). Gap junctional communication in morphogenesis. Progress in Biophysics and
675 Molecular Biology *94*, 186–206.

676 Lin, D., Boyle, D.L., and Takemoto, D.J. (2003). IGF-I-induced phosphorylation of connexin 43
677 by PKC gamma: regulation of gap junctions in rabbit lens epithelial cells. Invest Ophthalmol Vis
678 Sci *44*, 1160–1168.

679 Loew, L.M. (2007). Where does all the PIP2 come from? The Journal of Physiology *582*, 945–
680 951.

681 Mammano, F., and Bortolozzi, M. (2018). $Ca^{2+}$ signaling, apoptosis and autophagy in the
682 developing cochlea: milestones to hearing acquisition. Cell Calcium *70*, 117–126.

683 Martin, N., and Bernard, D. (2017). Calcium signaling and cellular senescence. Cell Calcium.

684 Nakai, J., Ohkura, M., and Imoto, K. (2001). A high signal-to-noise $Ca^{2+}$ probe composed of a
685 single green fluorescent protein. Nature Biotechnology *19*, 137–141.

686 Narciso, C.E., Contento, N.M., Storey, T.J., Hoelzle, D.J., and Zartman, J.J. (2017). Release of
687 applied mechanical loading stimulates intercellular calcium waves in *Drosophila* wing discs.
688 Biophysical Journal *113*, 491–501.

689 O'Connor, J.T., Stevens, A.C., Shannon, E.K., Akbar, F.B., LaFever, K.S., Narayanan, N.,
690 Hutson, M.S., and Page-McCaw, A. (2020). A protease-initiated model of wound detection.
691 BioRxiv 2020.12.08.415554.

692 Ohno, Y., and Otaki, J.M. (2015). Spontaneous long-range calcium waves in developing
693 butterfly wings. BMC Developmental Biology *15*, 17.

694 Orrenius, S., Zhivotovsky, B., and Nicotera, P. (2003). Calcium: Regulation of cell death: the
695 calcium–apoptosis link. Nature Reviews Molecular Cell Biology *4*, 552.

696 Perkins, L.A., Holderbaum, L., Tao, R., Hu, Y., Sopko, R., McCall, K., Yang-Zhou, D., Flockhart,
697 I., Binari, R., Shim, H.-S., et al. (2015). The transgenic RNAi project at Harvard Medical School:
698 resources and validation. Genetics *201*, 843–852.

699 Potter, C. (2001). Mechanisms of size control. Current Opinion in Genetics & Development *11*,
700 279–286.

701 Ratnaparkhi, A., Banerjee, S., and Hasan, G. (2002). Altered Levels of Gq Activity Modulate
702 Axonal Pathfinding in *Drosophila*. J. Neurosci. *22*, 4499–4508.

703 Restrepo, S., and Basler, K. (2016). *Drosophila* wing imaginal discs respond to mechanical
704 injury via slow InsP 3 R-mediated intercellular calcium waves. Nature Communications *7*,
705 12450.

706 Restrepo, S., Zartman, J.J., and Basler, K. (2014). Coordination of Patterning and Growth by
707 the Morphogen DPP. Current Biology *24*, R245–R255.

708 Richard, M., Bauer, R., Tavosanis, G., and Hoch, M. (2017). The gap junction protein Innexin3
709 is required for eye disc growth in *Drosophila*. Developmental Biology *425*, 191–207.

710 Ryerse, J.S. (1982). Gap junctions are non-randomly distributed in *Drosophila* wing discs.
711 Wilhelm Roux' Archiv *191*, 335–339.

712 Schöck, F., and Perrimon, N. (2002). Molecular Mechanisms of Epithelial Morphogenesis.
713 Annual Review of Cell and Developmental Biology *18*, 463–493.

714 Sneyd, J., Han, J.M., Wang, L., Chen, J., Yang, X., Tanimura, A., Sanderson, M.J., Kirk, V., and
715 Yule, D.I. (2017). On the dynamical structure of calcium oscillations. Proceedings of the
716 National Academy of Sciences 201614613.

717 Takeuchi, Y., Narumi, R., Akiyama, R., Vitiello, E., Shirai, T., Tanimura, N., Kuromiya, K.,
718 Ishikawa, S., Kajita, M., Tada, M., et al. (2020). Calcium Wave Promotes Cell Extrusion. Current
719 Biology *30*, 670-681.e6.

720 Vollmer, J., and Iber, D. (2016). An Unbiased Analysis of Candidate Mechanisms for the
721 Regulation of *Drosophila* Wing Disc Growth. Scientific Reports *6*, 39228.

722 Vollmer, J., Casares, F., and Iber, D. (2017). Growth and size control during development. Open
723 Biology *7*, 170190.

724 Warn-Cramer, B.J., and Lau, A.F. (2004). Regulation of gap junctions by tyrosine protein
725 kinases. Biochim Biophys Acta *1662*, 81–95.

726 Wei, C., Wang, X., Chen, M., Ouyang, K., Song, L.-S., and Cheng, H. (2009). Calcium flickers
727 steer cell migration. Nature *457*, 901.

728 Weir, M.P., and Lo, C.W. (1982). Gap junctional communication compartments in the
729 *Drosophila* wing disk. PNAS *79*, 3232–3235.

730 Weir, M.P., and Lo, C.W. (1985). An anterior/posterior communication compartment border in
731 engrailed wing discs: Possible implications for *Drosophila* pattern formation. Developmental
732 Biology *110*, 84–90.

733 Werz, C., Köhler, K., Hafen, E., and Stocker, H. (2009). The *Drosophila* SH2B family adaptor
734 Lnk acts in parallel to chico in the insulin signaling pathway. PLoS Genetics *5*, e1000596.

735 Wyss, C. (1982). Ecdysterone, insulin and fly extract needed for the proliferation of normal
736 *Drosophila* cells in defined medium. Experimental Cell Research *139*, 297–307.

737 Yamauchi, T. (2005). Neuronal $Ca^{2+}$/Calmodulin-Dependent Protein Kinase II—Discovery,
738 Progress in a Quarter of a Century, and Perspective: Implication for Learning and Memory.
739 Biological and Pharmaceutical Bulletin *28*, 1342–1354.

740 Zartman, J., Restrepo, S., and Basler, K. (2013). A high-throughput template for optimizing
741 *Drosophila* organ culture with response-surface methods. Development *140*, 667–674.

742